Article

Construction of Fe- and N-Doped Microporous Carbon from Ferrocene-Based Conjugated Microporous Polymers for Supercapacitive Energy Storage

Mohamed Gamal Mohamed,* Mohammed G. Kotp, Aya Osama Mousa, Yi-Shun Li, and Shiao-Wei Kuo*

Cite This: https://doi.org/10.1021/acsaem.4c02968

Read Online

ACCESS | Metrics & More | Article Recommendations | Supporting Information

ABSTRACT: The rising interest in conjugated microporous polymers (CMPs) as prospective electrode materials for supercapacitors (SCs) has been dampened by numerous obstacles. Many CMPs exhibit poor conductivity and substandard electrochemical properties, limiting their practical applications. In response to these issues, we successfully synthesized Fe- and N-doped microporous carbon-based materials from Py-BZFC-CMP and Py-PHFC-CMP through calcination and potassium hydroxide (KOH) activation at 800 °C. The resulting microporous carbons, designated as Py-BZFC-CMP-800 and Py-PHFC-CMP-800, demonstrated excellent attributes, including outstanding thermal stability with a T_{d10} up to 732 °C, and impressive char yields reaching 87 wt %. Furthermore, these materials exhibited large surface areas, peaking at 376 m^2 g^{-1}, and a significant total pore volume (PV_{total}) of up to 0.36 cm^3 g^{-1}. One remarkable material, Py-PHFC-CMP-800, produced through calcination and KOH activation at 800 °C, demonstrated exceptional electrochemical performance. It achieved a specific capacitance of 324 F g^{-1} at 0.5 A g^{-1}, rivaling some of the highest performing porous carbon materials reported to date. The Py-PHFC-CMP-800 demonstrated outstanding cycling stability, retaining 86% of its capacitance after 5000 charge–discharge cycles at 10 A g^{-1}. This project offers a significant advancement in the field of CMP-based materials by showcasing how rational precursor design and pyrolysis can lead to the creation of high-performance microporous carbons. The Fe and heteroatom doping approach enhances their functionality and opens up possibilities owing to their use in a valuable application, including efficient energy storage systems.
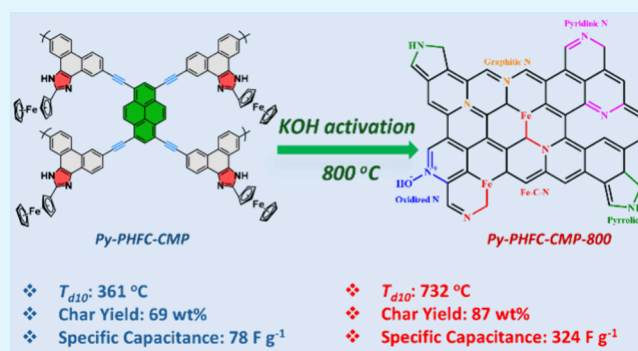
KEYWORDS: *ferrocene, pyrene, phenanthrene-9,10-dione, conjugated microporous polymers, microporous carbons, supercapacitor*

Py-PHFC-CMP → KOH activation 800 °C → Py-PHFC-CMP-800

- T_{d10}: 361 °C
- Char Yield: 69 wt%
- Specific Capacitance: 78 F g^{-1}

- T_{d10}: 732 °C
- Char Yield: 87 wt%
- Specific Capacitance: 324 F g^{-1}

■ INTRODUCTION

With climate change, environmental pollution, and the urgent need to enhance energy security becoming increasingly critical issues, significant progress has been made in the quest for clean and sustainable energy sources.[1−8] Numerous countries have allocated considerable resources and initiated extensive research efforts to advance clean and renewable energy technologies in response to these pressing challenges.[9−11] Notable examples of these initiatives include the advancement of energy storage, nuclear energy, and wind power, particularly in the realm of supercapacitors (SCs).[9−11] SCs are becoming a major area of interest for energy storage technologies due to their remarkable properties. They are known for their exceptional cycle life, consistent safety performance, high power density, and rapid charge–discharge capabilities, making them very appealing for a range of energy storage uses.[12−15] These characteristics position SCs as strong contenders in the area of energy preservation, although challenges such as limited

energy density still need to be addressed.[16,17] SCs are generally categorized into electrochemical double-layer capacitors (EDLCs) and pseudocapacitors.[18,19] Each type employs distinct energy storage and discharge processes, with EDLCs relying on the physical separation of charge and pseudocapacitors utilizing Faradaic reactions. Both categories contribute uniquely to the performance and applications of SCs, and ongoing research is focused on enhancing their efficiency and overcoming existing limitations to broaden their practical use.[18−20]

Conjugated microporous polymers (CMPs) stand out within the category of porous organic polymers (POPs) due to their intricate nanopore structures and extended π conjugation, making them highly unique and innovative materials.[21−25] Many C−N and C−C coupling processes are often necessary for the synthesis of CMPs,[22,23,25] with common methods including Schiff base formation oxidative polymerization, Buchwald amination, the Sonogashira coupling, cyclotrimerization, Yamamoto reactions, and Suzuki coupling.[22,23,25] CMPs are exceptionally versatile, finding applications in numerous fields such as organic light-emitting diodes (OLEDs), energy storage and conversion, biological systems, chemosensing, catalysis, and gas separation.[22,25−34] One of the key advantages of CMPs lies in their customizable frameworks, which allow for the modulation of π-conjugated segments, outstanding thermal stability, and structural tunability. CMPs offer several advantages over traditional electrode materials in supercapacitor applications, including wide availability and affordability. However, their effectiveness in energy storage is sometimes limited by issues like low electrical conductivity and weak redox activity.[35,36] The creation of materials using porous carbon has attracted a lot of interest because of their abundant resources and remarkable properties.[37,38] These materials are characterized by their adjustable pore structures, excellent thermal, mechanical, and chemical stability, high electrical conductivity, large surface areas, structural versatility, and substantial pore volumes.[39,40] These attributes make porous carbons highly useful in a variety of practical applications. They are extensively utilized in electromagnetic interference shielding, gas separation and capture, water treatment, catalysis, energy storage systems, and fuel cell technologies.[41−46]

The excellent porosity properties of porous carbon materials can be produced through calcination and KOH activation techniques, which are adaptable to a wide range of polymers. Some prominent examples of such polymers include CMPs, metal−organic frameworks (MOFs), and porous aromatic frameworks (PAFs).[47−51] For example, Mousa et al. synthesized Py-PDT POP-600) and evaluated its electrochemical properties. Py-PDT POP-600 exhibited an impressive capacitance of 550 F g^{-1} at 0.5 A g^{-1} and demonstrated good cyclic stability.[52] According to Mohamed et al, TPE-CPOP1−800 demonstrated a capacitance of 453 F g^{-1} (at 0.5 A g^{-1}).[53]

This research centered on producing microporous carbonaceous materials (derived from Py-BZFC-CMP and Py-PHFC-CMP) by employing the calcination and KOH activation at a high-temperature process at 800 °C to produce Py-BZFC-CMP-800 and Py-PHFC-CMP-800; respectively. The precursor materials used for this process were Py-BZFC-CMP and Py-PHFC-CMP, which were synthesized via Sonogashira polymerization with Py-T. The polymerization reaction involved the incorporation of either BZFC-2Br or PHFC-2Br as building blocks, contributing to the formation of the desired CMPs. A comprehensive investigation of the physical and chemical properties of these CMPs and their corresponding carbon materials was carried out using various analytical techniques. Additionally, the electrochemical studies were performed on both the CMP precursors (Py-BZFC-CMP and Py-PHFC-CMP) and the resultant MCs materials (Py-BZFC-CMP-800 and Py-PHFC-CMP-800) to evaluate their electrochemical performance, particularly in terms of their applicability for energy storage. Comprehensive analyses revealed

that the MC material Py-PHFC-CMP-800 displayed exceptional properties, achieving an impressive capacitance of 324 F g^{-1}. These findings highlight the enhanced performance of the Py-PHFC-CMP-800, over their precursor materials, making them promising candidates for both gas capture and SCs applications. These results not only demonstrate the possibility of the Py-PHFC-CMP-800 but also open new avenues for further research aimed at optimizing CMP-based carbons for advanced functional applications.

■ EXPERIMENTAL SECTION

Materials. 4,4′-Dibromobenzil (BZ-2Br, 90%), tetrakis-(triphenylphosphine)palladium(0) [Pd(PPh$_3$)$_4$, ≥99.99%], methanol (MeOH), acetic acid (AcOH, ≥99.7%), triethylamine (Et$_3$N, ≥99.5%), copper(I) iodide (CuI, 99%), ferrocenecarboxaldehyde (FC−CHO, 98%), ammonium acetate (CH$_3$COONH$_4$, 99.99%), and triphenylphosphine (PPh$_3$, 99%) were ordered from Sigma-Aldrich. Tetrahydrofuran (THF), DMF, and acetone were purchased from Acros. 1,3,6,8-Tetraethynylpyrene (Py-T) and 2,7-dibromo-phenan-threne-9,10-dione (PH-2Br) were synthesized according to methods described in the literature.[54−56]

Synthesis of BZFC-2Br. One g of BZ-2Br (2.7 mmol), 0.7 g of FC−CHO (4.675 mmol), 2.6 g of CH$_3$COONH$_4$ (33.73 mmol) were mixed with 10 mL of AcOH and refluxed at 110 °C for 2 days. Later, we sieved the resultant solid and rinsed it with H$_2$O and MeOH to remove any leftover reagents to produce BZFC-2Br as a black powder (0.91 g). FTIR (cm^{-1}, Figure S1): 3421.5 (NH), 3093.5, 1590.8 (C=C). ^{1}H NMR (ppm, Figure S2): 12.3 (NH), 7.63, 7.47, 4.92, 4.36, 4.12. High-resolution mass spectrometry of BZFC-2Br (C$_{25}$H$_{18}$Br$_2$FeN$_2$) is shown in Figure S3, (m/z): 560.9259. T_{d10}: 254 °C and weight residue at 800 °C: 31 wt % (Figure S4).

Synthesis of PHFC-2Br. PH-2Br (1 g, 2.73 mmol), 0.7 g of FC−CHO (4.675 mmol), 2.6 g of CH$_3$COONH$_4$ (33.73 mmol), and 10 mL of AcOH were refluxed under N$_2$ at 110 °C for 2 days. Upon completion, we sieved the resultant solid and rinsed it with MeOH and H$_2$O to obtain PHFC-2Br as a black powder (0.9 g). FTIR (cm^{-1}, Figure S5): 3333.3 (NH), 3089.9, 1587.6 (C=C). High-resolution mass spectrometry of PHFC-2Br (C$_{25}$H$_{16}$Br$_2$FeN$_2$) is shown in Figure S6, (m/z): 558.9102. T_{d10}: 257 °C and weight residue at 800 °C: 27 wt % (Figure S4).

Synthesis of Py-BZFC-CMP and Py-PHFC-CMP. Ten mL of DMF and 10 mL of Et$_3$N, BZ-2Br (0.37 g) or PHFC-2Br (0.38 g), PyT (0.2 g), PPh$_3$ (0.18 g), CuI (0.1 g), and Pd(PPh$_3$)$_4$ (0.77 g) under 110 °C for 3 days. Afterward, the solid was washed with THF, acetone, and MeOH. Finally, we put it in the vacuum oven to dry for 1 day to get the brown powder of Py-BZFC-CMP (0.35 g) and Py-PHFC-CMP (0.43 g) as a black solid.

Preparation of Py-BZFC-CMP-800 and Py-PHFC-CMP-800. The synthesized Py-BZFC-CMP (0.3 g) and Py-PHFC-CMP (0.3 g) were first calcined at 600 °C under a N$_2$ atmosphere for 3 h. Subsequently, 0.2 g each of calcined Py-BZFC-CMP and Py-PHFC-CMP was activated with 0.2 g of KOH at 800 °C for 6 h under a N$_2$ atmosphere. The resulting solid was then thoroughly washed with dilute HCl (2 N) to remove the excess KOH, followed by rinsing with H$_2$O and MeOH to ensure complete purification. This process yielded Py-BZFC-CMP-800 and Py-PHFC-CMP-800 as black solid materials. Inductively coupled plasma (ICP) tests were conducted to determine the Fe content in Py-BZFC-CMP, Py-PHFC-CMP, Py-BZFC-CMP-800, and Py-PHFC-CMP-800, which were found to be 0.77, 0.67, 0.81, and 0.69 wt %, respectively.

■ RESULTS AND DISCUSSION

Characterization of Py-BZFC-CMP, Py-PHFC-CMP, Py-BZFC-CMP-800, and Py-PHFC-CMP-800 Materials. The substantial surface area of porous organic polymers (POPs) makes them highly attractive for significantly enhancing the performance of SC electrodes. However, the low electrical

Scheme 1. Synthetic Approach for the Preparation of (a) BZFC-2Br, (b) PHFC-2Br Precursors from FC−CHO, (c) Py-BZFC, and (d) Py-PHFC-CMPs
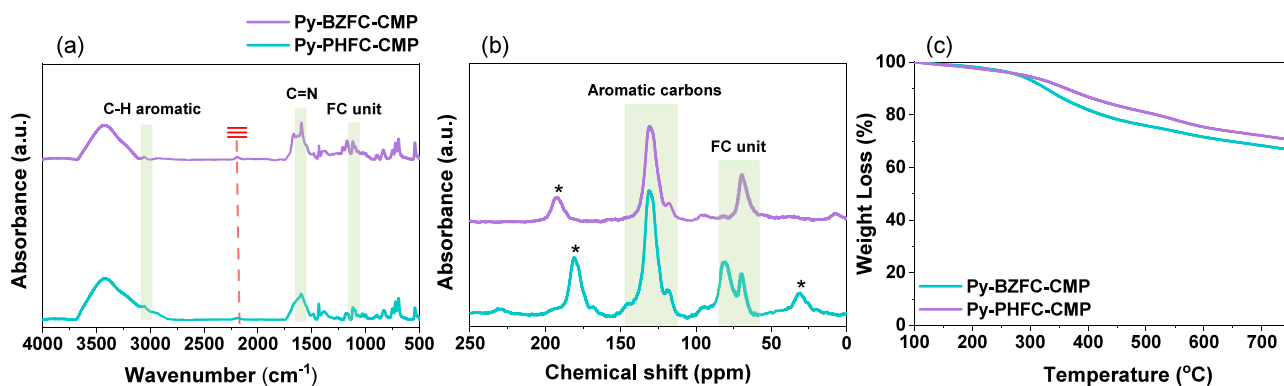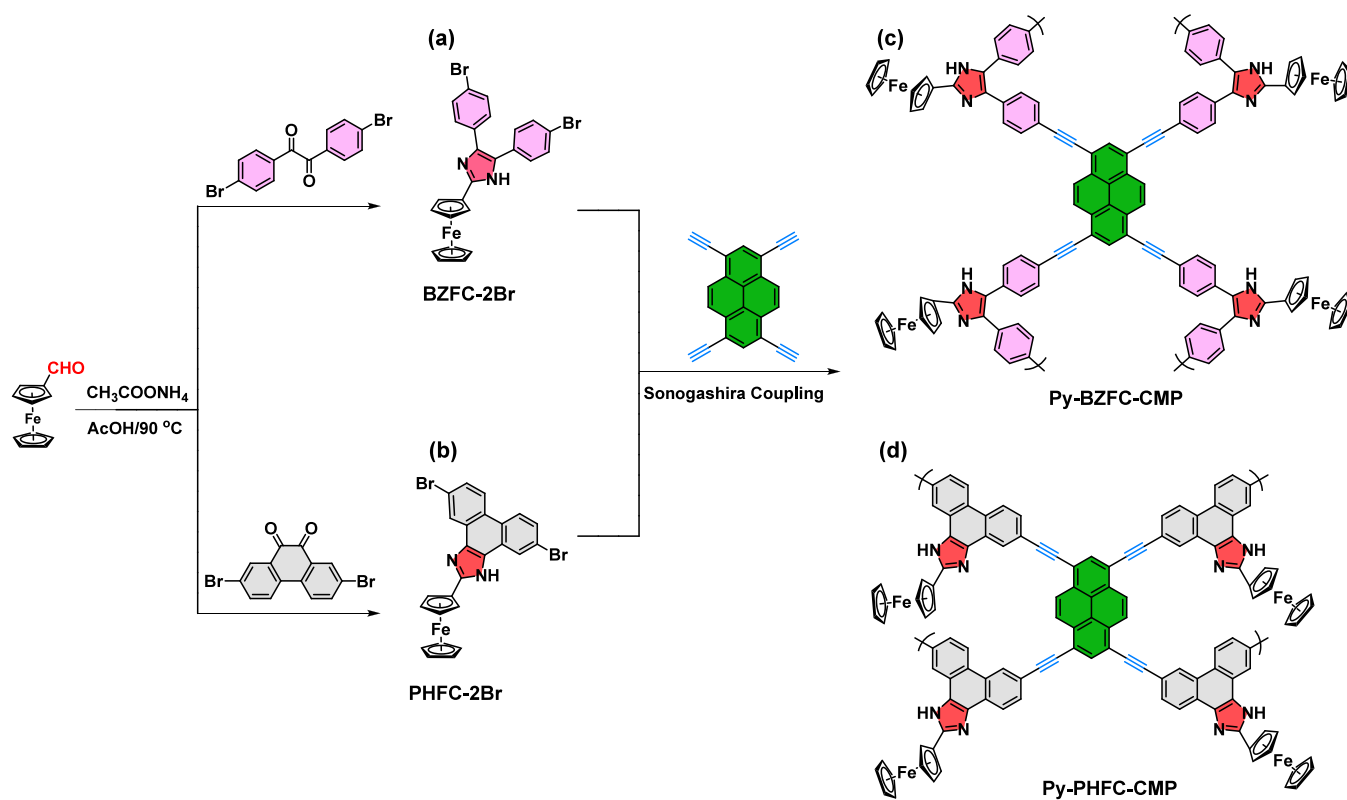
Figure 1. (a) FTIR spectra, (b) solid-state ^{13}C NMR, and (c) TGA analyses of Py-BZFC-CMP and Py-PHFC-CMP.

conductivity of many porous polymers limits their practical application. While conductivity can be improved by incorporating conductive materials, this approach alone may not fully address the issue. Recent studies have shown that converting porous polymers into their carbonaceous forms can effectively address the conductivity issue. This conversion greatly improves electrical mobility while retaining the polymer's original structure, resulting in electrodes with relatively high capacitance suitable for SCs.[57] In EDLCs, the accessibility of electrolyte ions to the electrode material is crucial for determining the SC's overall performance. Porous carbon materials are therefore frequently used for electrodes because of their superior electrical conductivity, robust mechanical properties, superior thermal and chemical stability, and tunable pore structures.[58,59] As one of the earliest recognized organometallic compounds, ferrocene (FC), and its related compounds were the focus of research that paved the way for

the field of organometallic chemistry.[60] The synthesis of FC is simpler and more cost-effective. Additionally, it offers a higher metal content compared to other organic compounds that bind to transition metals.[61] Its outstanding redox properties, unique photophysical behavior, and ability to facilitate charge separation have made it widely used in applications such as medical sensors and catalytic processes.[62,63] We synthesized two FC-based-CMPs using the Sonogashira coupling reaction. BZFC-2Br and PHFC-2Br were synthesized by reacting BZ-2Br and PH-2Br with FC−CHO in the presence of CH$_3$COONH$_4$ and AcOH. This reaction yielded a black solid for both BZFC-2Br and PHFC-2Br (Scheme 1a,b). Then, the Sonogashira coupling reaction involved reacting the Py-T with either BZFC-2Br or PHFC-2Br in a mixed solution of DMF and Et$_3$N, using Pd(PPh$_3$)$_4$ as the catalyst (Scheme 1c,d).
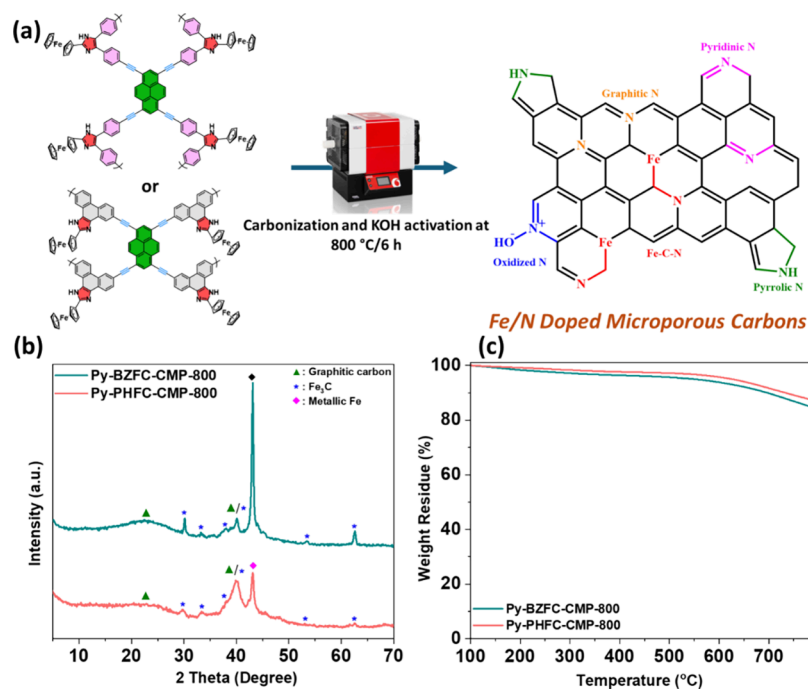
Figure 2. (a) Preparation of Py-BZFC-CMP-800 and Py-PHFC-CMP-800 from Py-BZFC-CMP and Py-PHFC-CMP precursors and (b) XRD and (c) TGA profiles of Py-BZFC-CMP-800 and Py-PHFC-CMP-800.

The reactions produced Py-BZFC-CMP, a brown powder, and Py-PHFC-CMP, a black solid. Their insoluble nature highlighted the significant cross-linking and polymerization of the FC-based CMPs in several organic solvents. The structures of the Py-BZFC and Py-PHFC-CMPs as displayed in Figure 1 were confirmed through FTIR analysis and solid-state ^{13}C NMR spectroscopy. The FTIR spectra of Py-BZFC and Py-PHFC-CMPs are presented in Figure 1a. Both FC-based CMPs displayed key absorption peaks: a peak at 2195 cm^{-1} corresponding to $-C\equiv C-$ and another at 3071 cm^{-1} associated with the vibration of C–H aromatics. Additionally, the spectra showed peaks in the range of 1119–1068 cm^{-1}, which are attributed to the cyclopentadiene rings (C=C stretching) in the FC unit. The vibrations of the aliphatic C–H group were detected at 2931 cm^{-1}. The disappearance of the C–Br bond, characteristic of the BZFC-2Br and PHFC-2Br monomers in the FTIR profiles for Py-BZFC and Py-PHFC-CMPs, alongside the emergence of the $-C\equiv C-$ signal in both Py-BZFC and Py-PHFC-CMPs, suggests the formation of interconnected polymer networks. The solid-state ^{13}C NMR spectra (Figure 1b) confirm the chemical composition of Py-BZFC-CMP and Py-PHFC-CMP. The overlapping carbon resonance peaks between 81.79 and 68.57 ppm strongly indicate the presence of $-C\equiv C-$ and FC units in both materials, consistent with findings from previous studies.[64,65] Additionally, broad resonances in the range of 115.02–145.41 ppm were attributed to aromatic carbons in both FC-based CMPs. Using thermogravimetric analysis (TGA), the thermal properties of Py-BZFC-CMP and Py-PHFC-CMP were investigated under N$_2$ (over a temperature range of 40–800 °C). The TGA curves, shown in Figure 1c, for Py-BZFC-CMP showed T_{d10} and char yield values of 326 °C and 66 wt %, while Py-PHFC-CMP had values of 361 °C and 69 wt %, respectively. The morphologies of the Py-BZFC and Py-PHFC-CMP were investigated using SEM images (Figures S7 and S8). SEM images revealed that the FC-based CMPs

consist of particles with a loosely agglomerated structure and varying shapes. Elemental mapping confirmed the uniform distribution of carbon and nitrogen throughout the porous Py-BZFC-CMP and Py-PHFC-CMP frameworks, as shown in Figures S7 and S8.

The XRD analysis, as shown in Figure S9, indicates that both Py-BZFC-CMP and Py-PHFC-CMP exhibit amorphous structures. After synthesis, the Py-BZFC-CMP and Py-PHFC-CMP were calcined and subsequently activated with KOH at 800 °C under a nitrogen atmosphere. This process produced Fe/N-doped microporous carbons, referred to as Py-BZFC-CMP-800 and Py-PHFC-CMP-800, respectively (Figure 2a). Figure 2b presents the XRD analysis of Py-BZFC-CMP-800 and Py-PHFC-CMP-800. Peaks around the $2\theta = 23°$ (002) plane and $2\theta = 40°$ (100) plane, respectively, exhibit certain characteristics of graphene, confirming the successful carbonization and KOH activation of the FC-based CMPs. The broadness of the (100) peak also indicates a disordered structure in this direction. Additionally, a peak at $2\theta = 43.1$ corresponds to the (110) plane of metallic iron (Fe), while other peaks suggest the presence of iron carbide (Fe$_3$C) within the Py-BZFC-CMP-800 and Py-PHFC-CMP-800 frameworks.[65,66] As shown by the TGA data in Figure 2c, the T_{d10} values and char yields were 696 °C and 85 wt % for Py-BZFC-CMP-800 and 732 °C and 87 wt % for Py-PHFC-CMP-800, respectively. It is evident from these findings that the materials' thermal stability considerably improved after calcination and KOH activation compared to the original materials, Py-BZFC and Py-PHFC-CMPs, as seen in Figure 1c.

To better understand and investigate the structural composition of the Py-BZFC-CMP-800 and Py-PHFC-CMP-800 frameworks, XPS analysis was conducted to examine the elemental composition and bonding ratios. Drawing on previous research related to nitrogen and iron-doped carbon materials, we performed peak deconvolution of the relevant elemental functional groups, as depicted in Figure 3a–h. The
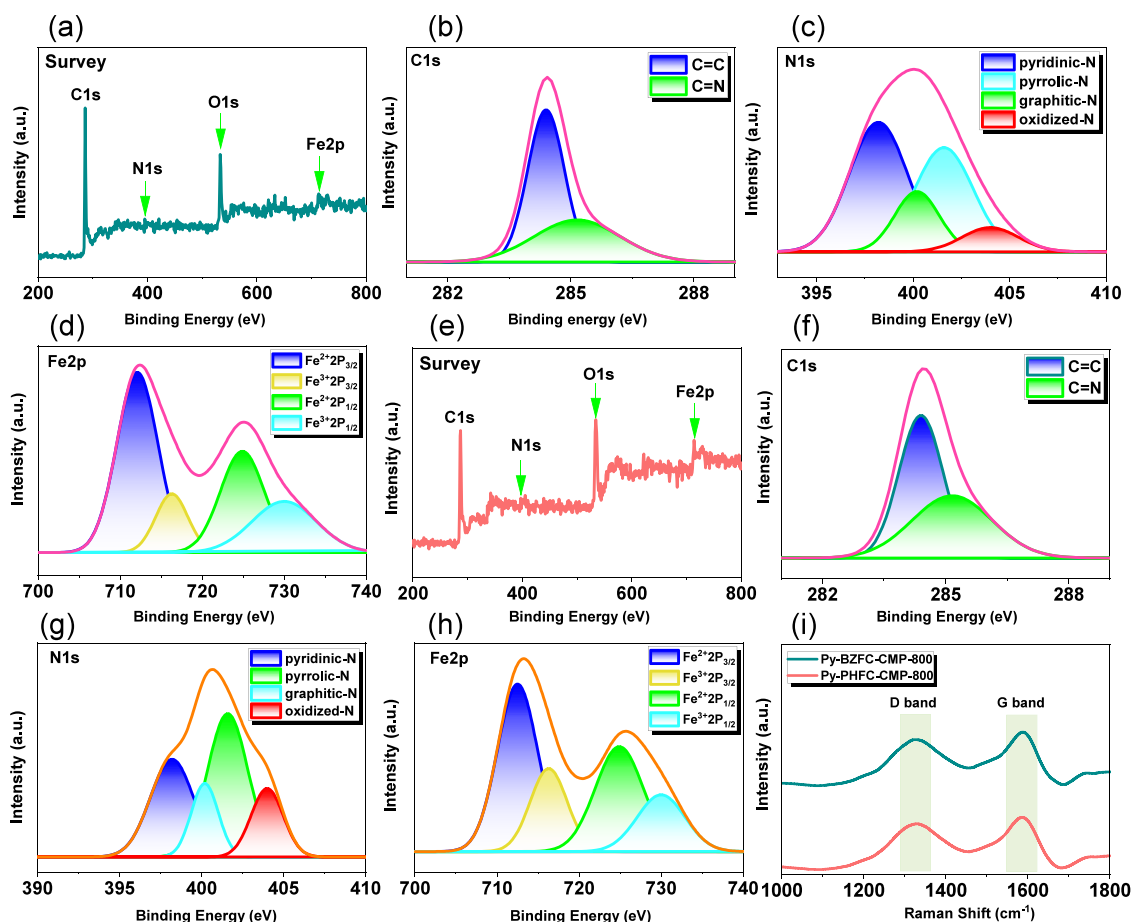
Figure 3. XPS survey and XPS fitting results of (a, b, c, d) Py-BZFC-CMP-800 and (e, f, g, h) Py-PHFC-CMP-800 and (i) Raman spectra of Py-BZFC-CMP-800 and Py-PHFC-CMP-800.

XPS survey spectra for both Py-BZFC-CMP-800 and Py-PHFC-CMP-800, shown in Figure 3a−e, reveal characteristic peaks for carbon, nitrogen, oxygen, and iron at approximately 290, 400, 532, and 700−740 eV, respectively.[67] In the C 1s patterns of the Py-BZFC-CMP-800 and Py-PHFC-CMP-800, the primary signal at 284.4 eV corresponds to C=C, indicating the presence of aromatic rings and a graphite-like structure as the main component. Additionally, the C=N bond is also significant, appearing at a binding energy of 285.16 eV, as shown in Figure 3b,f. In their N 1s profiles, nitrogen is composed of four functional groups: the binding energies of pyridinic N (N-6), pyrrolic N (N-5), graphitic N (N-Q), and oxidized N (N-X), appearing at 398.2, 400.2, 401.6, and 404.0 eV, respectively,[67] as shown in Figure 3c,g. A higher combined ratio of N-5 and N-6 indicates a greater likelihood of forming Fe−N−C, which provides redox-active sites and increases the efficiency of these materials' electrochemical process. Finally, in the Fe 2p spectra of Py-BZFC-CMP-800 and Py-PHFC-CMP-800, the Fe^{2+} $2p_{3/2}$, Fe^{3+} $2p_{3/2}$, Fe^{2+} $2p_{1/2}$, and Fe^{3+} $2p_{1/2}$ peaks appear at 712.1, 716.3, 724.9, and 730 eV, respectively,[67] as shown in Figure 3d,h. These peaks indicate the presence of different oxidation states of iron, corresponding to the various oxidation configurations. Following KOH activation, the presence of iron and the synthesis of Fe−N−C are confirmed by the Fe 2p signals.[67] The Raman spectra of Py-BZFC-CMP-800 and Py-PHFC-CMP-800 (Figure 3i) show characteristic carbon material peaks: the G band (1580 cm^{-1}) for ordered graphitic

structures and the D band (1340 cm^{-1}) for structural defects. The intensity ratio (I_D/I_G) reveals defect density, with Py-BZFC-CMP-800 having a ratio of 0.87 and Py-PHFC-CMP-800 with a lower ratio of 0.73. This suggests that Py-PHFC-CMP-800 has fewer defects and a more ordered structure.[67]

N_2 sorption isotherms were conducted at 77 K to analyze the porosity characteristics of the FC-based CMPs and their corresponding microporous carbon derivatives (Py-BZFC-CMP-800 and Py-PHFC-CMP-800), as shown in Figure 4 and Figure S10. The type-1 isotherm profiles of Py-BZFC-CMP-800 and Py-PHFC-CMP-800, displaying rapid nitrogen absorption at low pressure and increasing adsorption at higher pressures, are consistent with the IUPAC classification. As indicated in Figure 4a, both micropores and mesopores are likely present in both samples. The Py-BZFC-CMP exhibited a BET surface area of 15 m^2 g^{-1} (Figure S10a), while its MC counterpart, Py-PHFC-CMP-800, showed a significantly higher BET surface area of 367 m^2 g^{-1}. Similarly, the Py-PHFC-CMP had a surface area of 14 m^2 g^{-1}, which increased to 376 m^2 g^{-1} after carbonization and KOH activation. These results suggest that the noncarbonized CMPs (Py-BZFC-CMP and Py-PHFC-CMP), with their lower surface areas, are likely to have reduced electrochemical performance compared to their microporous carbon (MC) forms. Additionally, the pore sizes of the FC-based CMPs, Py-BZFC-CMP-800 and, Py-PHFC-CMP-800 were analyzed using N_2 sorption isotherms and NLDFT. As shown in Figure 4b and Figure S10b, the pore sizes were centered at 2.44, 2.47, 1.2, and 1.47 nm for Py-
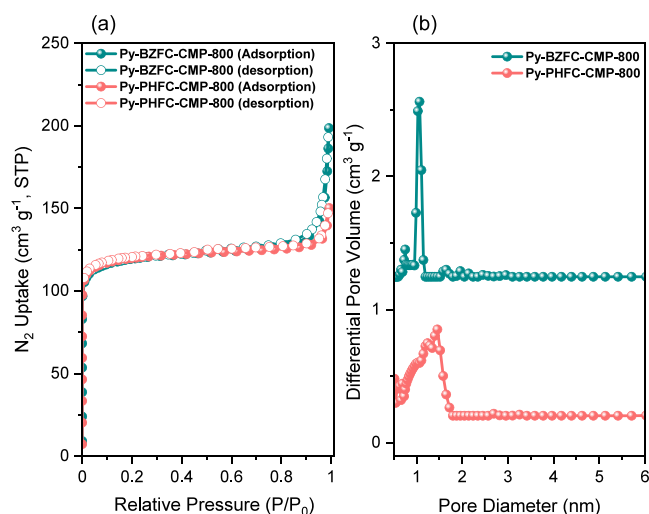
Figure 4. (a) Nitrogen sorption isotherms and (b) pore size distribution curves of Py-BZFC-CMP-800 and Py-PHFC-CMP-800.

BZFC-CMP, Py-PHFC-CMP, Py-BZFC-CMP-800, and Py-PHFC-CMP-800, respectively. The corresponding pore volumes were 0.17, 0.03, 0.43, and 0.36 cm^3 g^{-1} for Py-BZFC-CMP, Py-PHFC-CMP, Py-BZFC-CMP-800, and Py-PHFC-CMP-800, respectively.

The SEM images for Py-BZFC-CMP-800 (Figure 5a,b) show a structure composed of aggregated small spheres, while Py-PHFC-CMP-800 (Figure 5c,d) exhibits a sheet-like

morphology. Elemental analysis through SEM-EDS mapping further confirmed the presence of C (red), N (green), and O (white) within both materials (Figure 5e–j), demonstrating the distribution of these elements in Py-BZFC-CMP-800 and Py-PHFC-CMP-800. The TEM images of both Py-BZFC-CMP-800 and Py-PHFC-CMP-800 (Figure 5k,l and Figure S11) reveal the well-dispersed Fe-based particles embedded within their porous frameworks. This dispersion underscores the effective integration of the nanoparticles within the materials. Furthermore, the TEM observations align closely with the XRD and XPS data (Figures 2b and 3), further corroborating the structural and compositional analysis.

Electrochemical Performance of Py-BZFC-CMP, Py-PHFC-CMP, Py-BZFC-CMP-800, and Py-PHFC-CMP-800. The electrochemical properties of the Py-BZFC-CMP, Py-PHFC-CMP, Py-BZFC-CMP-800, and Py-PHFC-CMP-800 were assessed using a three-electrode setup, including cyclic voltammetry (CV) and galvanostatic charge–discharge (GCD) techniques in a 6 M KOH alkaline electrolyte. The electrolyte's use of 6 M KOH is common in SC studies due to its high ionic conductivity, which enhances charge storage processes. By varying the sweep rates during the CV experiments, the rate capability and charge storage mechanisms of the materials could be analyzed. Higher sweep rates help assess performance under high-power conditions, while lower sweep rates provide more detailed insights into the underlying electrochemical processes. This comprehensive approach enabled a thorough investigation of the materials' potential for energy storage applications. The selection of building
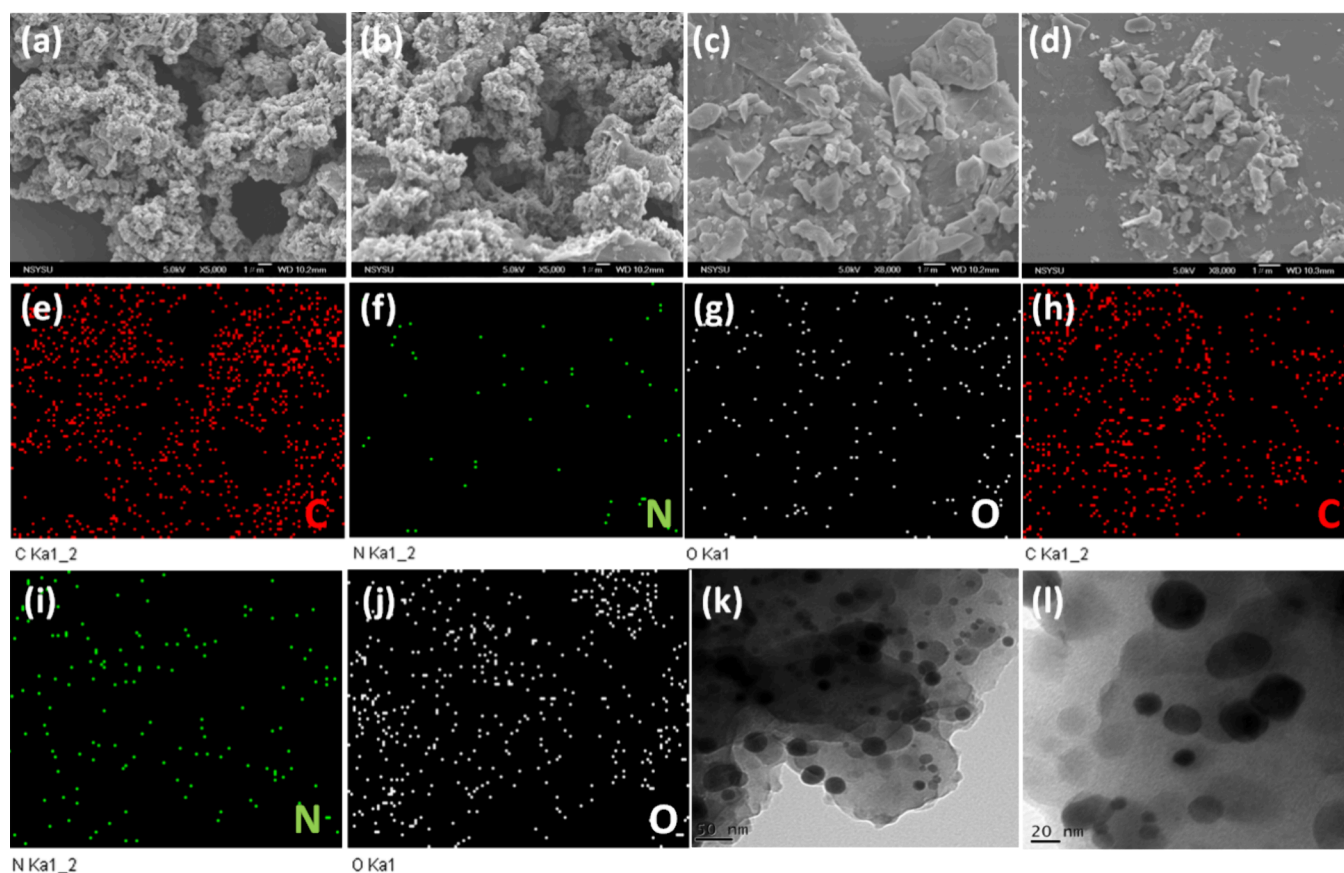
Figure 5. (a−d) SEM images, (e−j) SEM-EDS images, and (k, l) TEM images of (a, b, e, f, g, k) Py-BZFC-CMP-800 and (c, d, h, i, j, l) Py-PHFC-CMP-800.
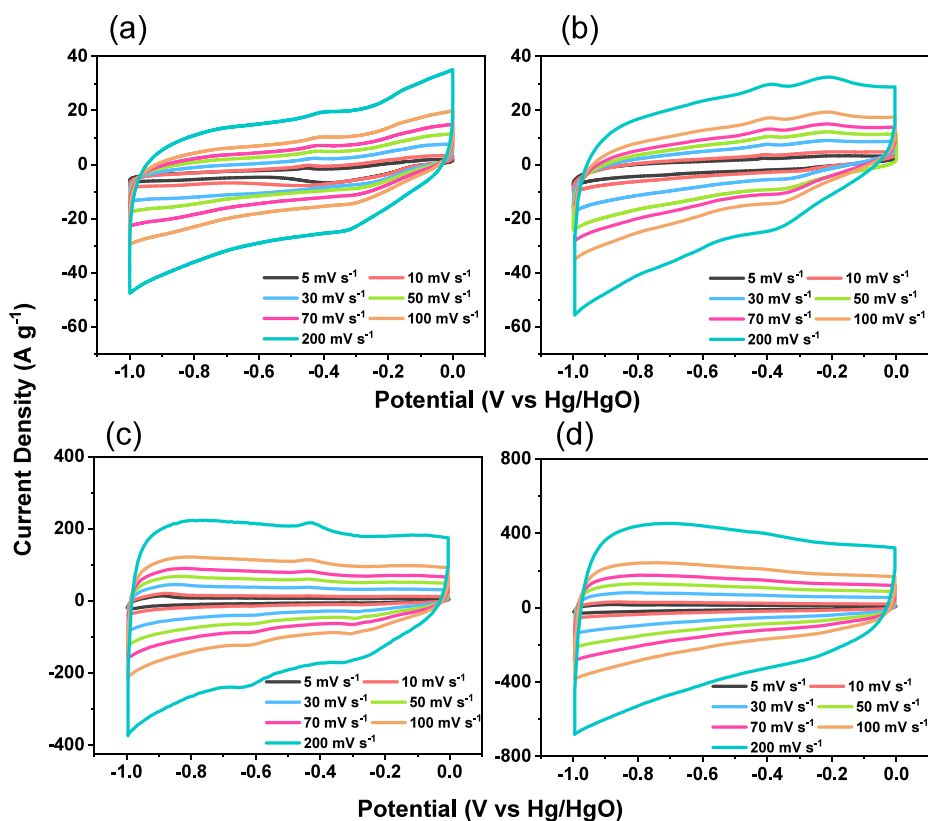
Figure 6. CV profiles of (a) Py-BZFC-CMP, (b) Py-PHFC-CMP, (c) Py-BZFC-CMP-800, and (d) Py-PHFC-CMP-800.
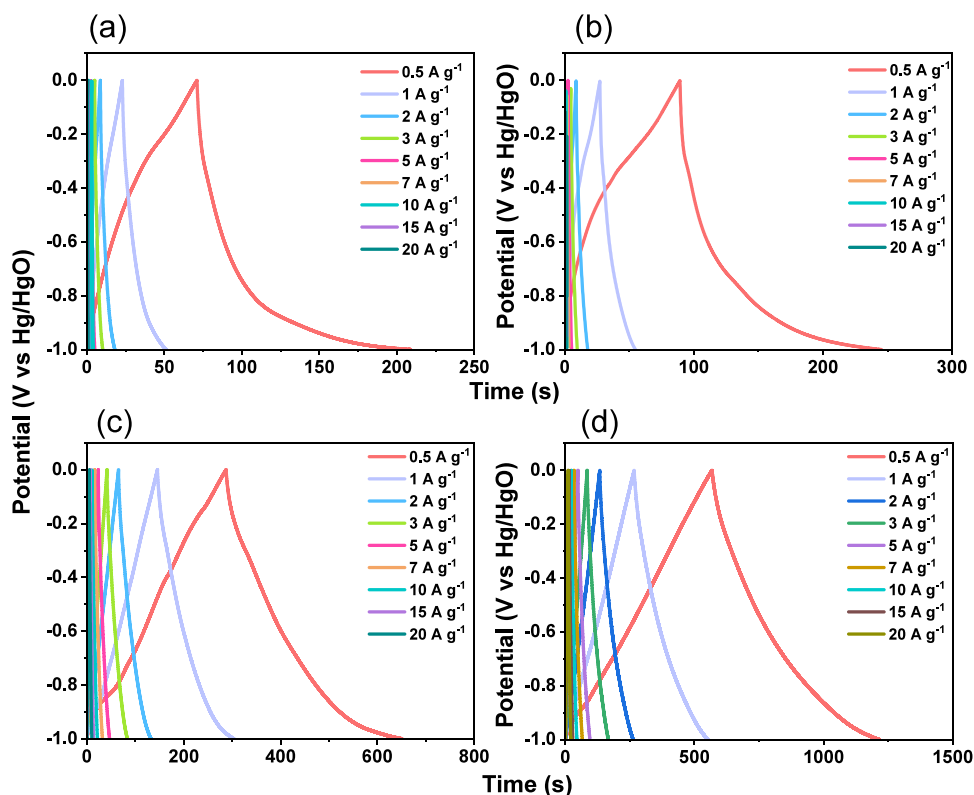
Figure 7. GCD profiles of (a) Py-BZFC-CMP, (b) Py-PHFC-CMP, (c) Py-BZFC-CMP-800, and (d) Py-PHFC-CMP-800.

blocks in our CMPs is crucial for optimizing their electrochemical performance. First, the pyrene (Py) units serve as a fixed component, providing a rigid and planar structure that

enhances π conjugation and charge delocalization along the polymer backbone. This structural stability supports efficient charge transfer. Second, ferrocene (FC) moieties, known for
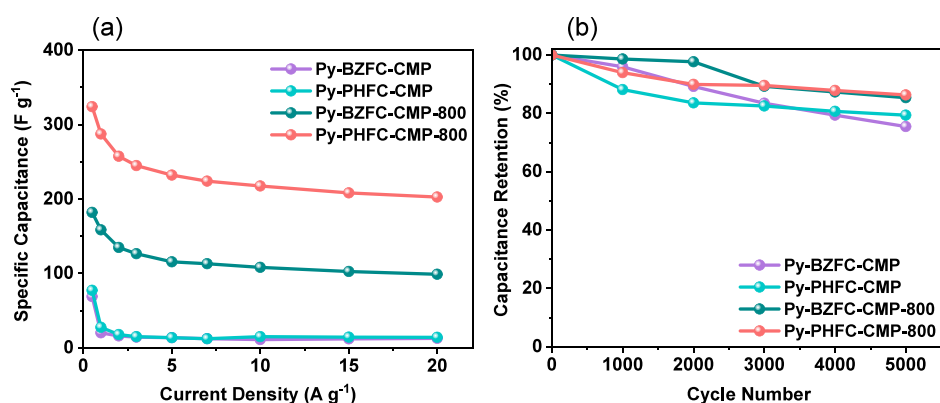
Figure 8. (a) Specific capacitance and (b) capacitance retention profiles of Py-BZFC-CMP, Py-PHFC-CMP, Py-BZFC-CMP-800, and Py-PHFC-CMP-800.

their redox-active properties, contribute to the pseudocapacitive behavior of the CMPs, resulting in higher specific capacitance compared to materials that rely solely on electric double-layer capacitance (EDLC). Third, the inclusion of 4,5-diphenyl-1H-imidazole and 1H-phenanthro[9,10-d]imidazole linkers introduce additional aromatic rings, extending π conjugation and increasing the available surface area for charge storage. This extended conjugation is beneficial for electrochemical performance. The CV curves of the Py-BZFC and Py-PHFC-CMPs, Py-BZFC-CMP-800, and Py-PHFC-CMP-800 (Figure 6a−d), measured at scan rates between 5 and 200 mV s^{-1}, show a quasi-rectangular shape, indicative of capacitive behavior. However, small humps or peaks within these curves suggest that additional electrochemical processes are occurring alongside the capacitive response. These humps are likely linked to the redox activity of the ferrocene units, which undergo reversible oxidation and reduction reactions. A key observation from the CV measurements is the significant increase in current density for the Py-BZFC-CMP-800 (Figure 6c) and Py-PHFC-CMP-800 (Figure 6d) compared to Py-BZFC-CMP and Py-PHFC-CMP. This improvement is primarily due to the increased surface area and enhanced electrical conductivity resulting from the KOH activation.

The GCD tests conducted on Py-BZFC-CMP, Py-PHFC-CMP, Py-BZFC-CMP-800, and Py-PHFC-CMP-800 (Figure 7a−d) at various current densities (ranging from 0.5 to 20 A g^{-1}) reveal distinct triangular shapes in the discharge profiles, with a slight curvature.[68] This triangular shape is indicative of both capacitive and pseudocapacitive behaviors, where the rapid charge and discharge processes are reflected in the current response. Notably, Py-PHFC-CMP (Figure 7b) exhibits a longer discharge time compared to Py-BZFC-CMP (Figure 7a), which correlates with its higher specific capacitance of 78 F g^{-1} compared to 69 F g^{-1} for Py-BZFC-CMP (Figure 8a). This higher specific capacitance in Py-PHFC-CMP can be attributed to its superior structural properties, including enhanced charge delocalization and increased redox activity provided by the 1H-phenanthro-[9,10-d]imidazole linker. This structural advantage promotes more efficient electron transfer and improved ion accessibility during charge−discharge cycles, enabling greater charge storage capacity. Additionally, both CMPs incorporate FC units that contribute to their pseudocapacitive behavior. However, the specific arrangement of these units and the electronic interactions in Py-PHFC-CMP may allow for more efficient redox reactions, leading to higher capacitance. The

phenanthroimidazole structure could also stabilize the oxidation state of ferrocene, further enhancing the overall charge storage mechanism. Notably, the Py-BZFC-CMP-800 and Py-PHFC-CMP-800 exhibit significantly higher discharge times compared to their pristine counterparts, leading to impressive specific capacitance values of 182 and 324 F g^{-1} at 0.5 A g^{-1} for Py-BZFC-CMP-800 and Py-PHFC-CMP-800 (Figure 8a). The increase in specific capacitance can be attributed to several factors. First, the KOH activation process improved the porosity of the CMPs, providing more active sites for ion adsorption and charge storage and allowing for greater electrolyte penetration and improved access to the redox-active sites, which is critical for achieving higher capacitance. The specific capacitance retention (after 5000 charge−discharge cycles at 10 A g^{-1}) is a key indicator of the long-term durability and cycling efficiency of supercapacitor electrode materials, reflecting their ability to sustain performance over prolonged use. For the pristine Py-BZFC-CMP and Py-PHFC-CMP, alongside the Py-BZFC-CMP-800 and Py-PHFC-CMP-800, the capacitance retention values are 71, 81, 85, and 86%, respectively (Figure 8b).

These figures elucidate the proportion of initial specific capacitance that is preserved post prolonged cycling, a key determinant in evaluating the endurance and operational integrity of supercapacitor materials over extended usage durations. Interestingly, our Py-PHFC-CMP-800 electrode demonstrates exceptional performance as an SC electrode, especially when compared to other reported carbon materials (Table S1). With a specific capacitance of 324 F g^{-1}, it significantly stands out in its category. This high value can be attributed to the material's unique structure, which combines an optimized pore size distribution and a nitrogen-rich framework. These characteristics enhance ion accessibility and promote better electrochemical interactions, leading to superior energy storage capabilities.

The capacitive contributions to the total capacity of the Py-BZFC and Py-PHFC-CMPs, along with Py-BZFC-CMP-800 and Py-PHFC-CMP-800, were quantitatively evaluated using the provided equations. Specifically, eq 1 delineates the relationship between the current $i(v)$ at a constant potential v, where k_1v represents the current stemming from diffusion-controlled processes and $k_2v^{1/2}$ represents the current generated by capacitive processes. This distinction between current contributions enables a more detailed understanding of the role that each mechanism plays in the overall electrochemical performance of these materials.[69,70]
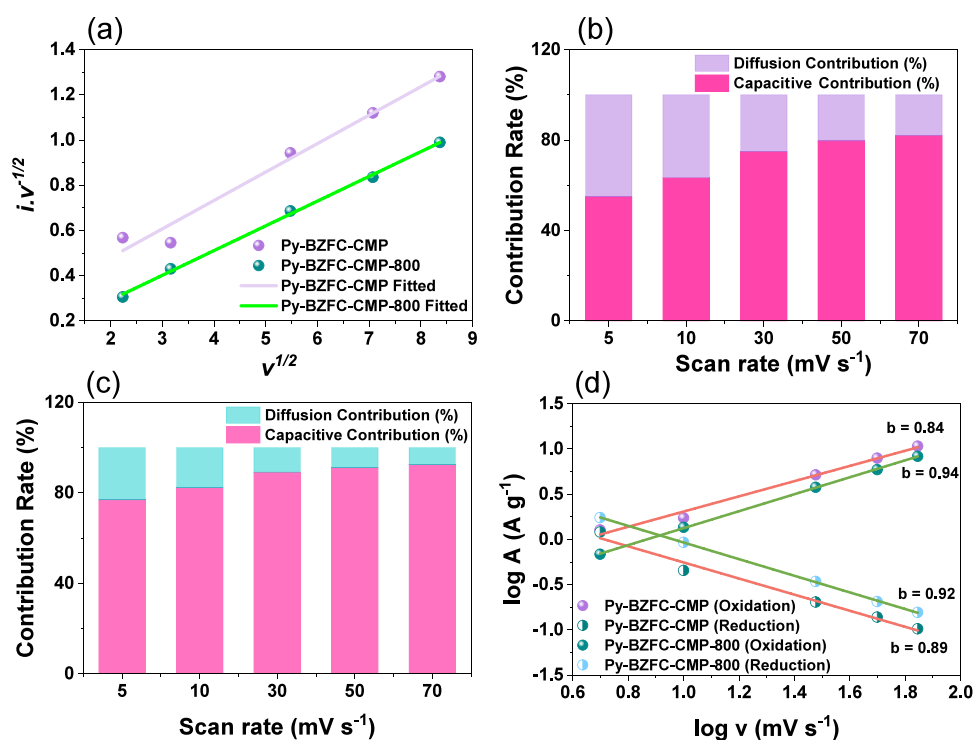
Figure 9. Relationships between $V^{1/2}$ versus $iv^{1/2}$ (a), capacitive and diffusion contributions incorporated under a variety of sweep rates (b, c), and relationships between the log v and those anodic and cathodic currents (d) of the Py-BZFC-CMP and Py-BZFC-CMP-800.
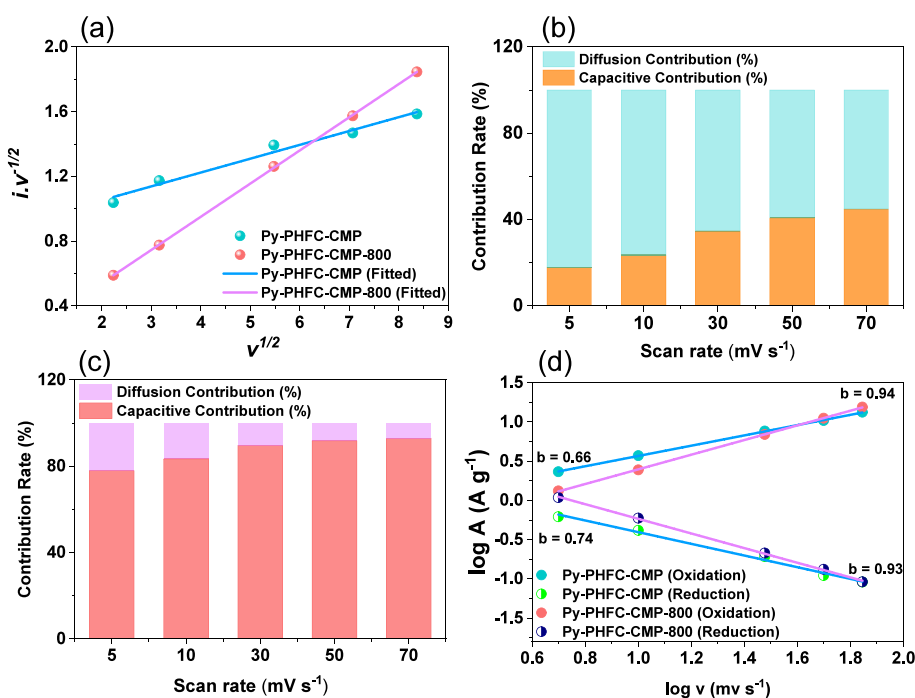

Figure 10. Relationships between $V^{1/2}$ versus $iv^{1/2}$ (a), capacitive and diffusion contributions incorporated under a variety of sweep rates (b, c), and relationships between the log v and those anodic and cathodic currents (d) of the Py-PHFC-CMP and Py-PHFC-CMP-800.

$$i(v) = k_1 v + k_2 v^{1/2} \tag{1}$$

This equation indicates that the total current $i(v)$ is a combination of two components: one that is linearly dependent on the potential v (associated with diffusion processes) and another that is dependent on the square root of the potential (associated with capacitive processes) as shown in eq 2:

$$\frac{i(v)}{v^{1/2}} = k_1 v^{1/2} + k_2 \tag{2}$$

By rearranging eq 1 into eq 2, the slope and intercept can be determined graphically. The slope corresponds to k_1, which quantifies the diffusion-controlled current, while the intercept represents k_2, which quantifies the capacitive current. This graphical representation allows for the extraction of values for

I
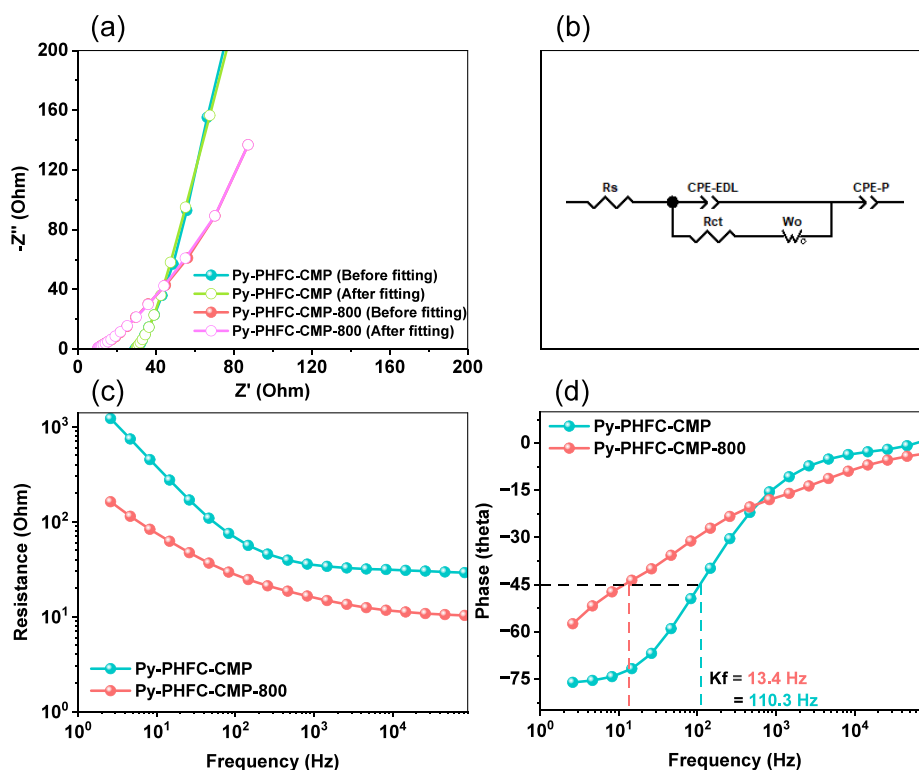
Figure 11. EIS curves: (a) Nyquist plots and (b) equivalent fitted circuit, (c) Bode plot of frequency-dependent resistance (magnitude), and (d) Bode plot of frequency-dependent phase angles of Py-PHFC-CMP and Py-PHFC-CMP-800.

k_1 and k_2 based on experimental data, as illustrated in Figures 9a and 10a.

The results indicate a significant increase in the capacitive contribution to the total current as the scan rate rises from 5 to 70 mV s^{-1}. The capacitive contribution for the Py-BZFC-CMP is 82.09% (Figure 9b), while the Py-BZFC-CMP-800 demonstrates an even higher capacitive contribution of 92.56% (Figure 9c). This suggests that the carbonization process enhances the material's ability to store charge through capacitive mechanisms, likely due to improvements in the surface area and conductivity, which enable faster ion transport and greater charge accumulation at the electrode interface.

In contrast, the Py-PHFC-CMP exhibits a lower capacitive contribution of 44.82% (Figure 10b) at the same scan rate, though its activated form, Py-PHFC-CMP-800, shows a substantial increase to 92.96% (Figure 10c). This indicates that, while the pristine Py-PHFC-CMP has inherent limitations in capacitive behavior, the KOH activation process significantly enhances its performance. The presence of the 1H-phenanthro[9,10-d]imidazole linker in the Py-PHFC-CMP may initially hinder ion diffusion and charge transfer, but carbonization likely strengthens its structural integrity and boosts conductivity, resulting in improved capacitive behavior. To further analyze the capacitive contributions of the FC-CMPs and their activated forms (Py-BZFC-CMP-800 and Py-PHFC-CMP-800), the power equation (eq 3) was employed to explore the relationship between i and v. This analysis offers deeper insights into how capacitive mechanisms contribute to the overall electrochemical performance.

$$i = av^b \qquad (3)$$

In this equation, a and b are constants, where a represents the proportionality factor and b indicates the nature of the

charge storage mechanism. The value of b provides crucial insights into whether the current response is dominated by diffusion or capacitance. The b values determined for the Py-BZFC-CMP, Py-PHFC-CMP, Py-BZFC-CMP-800, and Py-PHFC-CMP-800 reflect the relative contributions of diffusion and capacitive mechanisms to their electrochemical performance. The anodic and cathodic peaks of Py-BZFC-CMP exhibit approximate b values of 0.84 and 0.89, respectively (Figure 9d), indicating that the charge storage mechanism is mostly capacitive, although diffusion processes still play a role. The Py-BZFC-CMP-800 exhibits slightly higher b values, with 0.94 and 0.92 for the anodic and cathodic peaks (Figure 9d), demonstrating an even stronger capacitive contribution compared to Py-BZFC-CMP. This enhancement is attributed to the increased surface area and improved conductivity achieved through KOH activation, which enables faster charge accumulation at the electrode surface. In contrast, the Py-PHFC-CMP shows lower b values, with 0.66 for the anodic peak and 0.74 for the cathodic peak (Figure 10d), indicating a more diffusion-controlled process. This suggests that the charge storage in pristine Py-PHFC-CMP is less capacitive, likely due to structural constraints that impede ion transport. However, the Py-PHFC-CMP-800 shows significantly higher b values of 0.94 and 0.93 for the anodic and cathodic peaks (Figure 10d). Analyzing the b values offers critical insights into the electrochemical properties of these CMPs. Higher b values closer to 1 indicate that the materials are well-suited for applications requiring rapid charge and discharge capabilities, such as in supercapacitors. The noticeable increase in b values for the Py-BZFC-CMP-800 and Py-PHFC-CMP-800 compared to their pristine forms highlights the effectiveness of carbonization in optimizing their electrochemical performance,

particularly by enhancing their capacitive charge storage abilities.

The electrochemical characteristics of the Py-PHFC-CMP and Py-PHFC-CMP-800 in a three-electrode configuration were assessed using electrochemical impedance spectroscopy (EIS). The Nyquist plots for Py-PHFC-CMP and Py-PHFC-CMP-800, displayed in Figure 11a, reveal their electrochemical behavior, with the corresponding fitted equivalent circuit model shown in Figure 11b. This model includes key components such as series resistance (R_s), charge transfer resistance (R_{ct}), constant phase elements (CPEs) representing electric double-layer capacitance (CPE-EDL) and pseudocapacitance (CPE-P), and a Warburg element (Z_w) to account for ion diffusion effects. The fitted data indicate that the ohmic resistances for Py-PHFC-CMP and Py-PHFC-CMP-800 are 29.68 Ω and 9.20 Ω, respectively (Table S2). This significant reduction in ohmic resistance—nearly 3-fold—demonstrates the enhanced electrochemical performance of the Py-PHFC-CMP-800 compared to Py-PHFC-CMP. However, the charge transfer resistance shows an inverse trend: Py-Fc-Phthra-800 CMP exhibits a higher Rct of 100.2 Ω, compared to 8.45 Ω for Py-PHFC-CMP. This suggests that while carbonization substantially reduces ohmic resistance, it increases charge transfer resistance, indicating a complex effect of the process on the materials' electrochemical behavior. Nevertheless, both Py-PHFC-CMP and Py-PHFC-CMP-800 exhibit potential as electrodes for energy storage applications. The Bode plots in Figure 11c illustrate the frequency-dependent impedance magnitude for both Py-PHFC-CMP and Py-PHFC-CMP-800, displaying sloped lines with negative gradients at lower frequencies and reduced resistance at higher frequencies, confirming the superior capacitive performance of both Py-PHFC-CMP and Py-PHFC-CMP-800. Additionally, the knee frequencies for Py-PHFC-CMP and Py-PHFC-CMP-800 are 110.26 and 13.39 Hz, respectively (Figure 11d), which highlights their rate capabilities. The lower knee frequency of Py-PHFC-CMP-800 suggests improved rate performance, further indicating its suitability for a high-rate energy storage system.

CONCLUSIONS

In this study, a simple Sonogashira reaction was employed to synthesize FC-based CMPs, followed by their carbonization and KOH activation through high-temperature processing to create advanced Fe/N-doped microporous carbon materials. The resulting Py-BZFC-CMP-800 and Py-PHFC-CMP-800 were thoroughly characterized using a variety of analytical techniques including BET, TGA, SEM, and TEM. These analyses revealed several remarkable properties in the Py-PHFC-CMP-800, such as an impressive specific surface area of 376 m² g⁻¹, with an exceptional T_{d10} of 732 °C and a high char yield of 87 wt %, and a well-defined microporous carbon structure. Notably, the material Py-PHFC-CMP-800 achieves a specific capacitance of 324 F g⁻¹ at 0.5 A g⁻¹. These studies highlight the substantial benefits of CMP precursors and heteroatom doping in microporous carbons, significantly enhancing supercapacitor performance.

ASSOCIATED CONTENT

Ⓢ Supporting Information

The Supporting Information is available free of charge at https://pubs.acs.org/doi/10.1021/acsaem.4c02968.

Electrochemical measurements; FTIR, ¹H NMR, ¹³C NMR, and HR mass spectrometry for BZFC-2Br and PHFC-2Br; SEM and SEM-EDS imaging; XRD and BET analyses for Py-BZFC-CMP and Py-PHFC-CMP; high-resolution TEM imaging for Py-BZFC-CMP-800 and Py-PHFC-CMP-800; comparison of the Py-BZFC-CMP, Py-PHFC-CMP, Py-BZFC-CMP-800, and Py-PHFC-CMP-800 supercapacitor performance with the electrodes that have been previously described and fitted EIS data of Py-PHFC-CMP and Py-PHFC-CMP-800 with characteristic values (in the three-electrode system) (PDF)

AUTHOR INFORMATION

Corresponding Authors

Mohamed Gamal Mohamed − *Department of Materials and Optoelectronic Science, Center for Functional Polymers and Supramolecular Materials, National Sun Yat-Sen University, Kaohsiung 804, Taiwan; Department of Chemistry, Faculty of Science, Assiut University, Assiut 71516, Egypt;* Ⓞ orcid.org/0000-0003-0301-8372; Email: mgamal.eldin34@gmail.com

Shiao-Wei Kuo − *Department of Materials and Optoelectronic Science, Center for Functional Polymers and Supramolecular Materials, National Sun Yat-Sen University, Kaohsiung 804, Taiwan; Department of Medicinal and Applied Chemistry, Kaohsiung Medical University, Kaohsiung 807, Taiwan;* Ⓞ orcid.org/0000-0002-4306-7171; Email: kuosw@faculty.nsysu.edu.tw

Authors

Mohammed G. Kotp − *Department of Materials and Optoelectronic Science, Center for Functional Polymers and Supramolecular Materials, National Sun Yat-Sen University, Kaohsiung 804, Taiwan*

Aya Osama Mousa − *Department of Materials and Optoelectronic Science, Center for Functional Polymers and Supramolecular Materials, National Sun Yat-Sen University, Kaohsiung 804, Taiwan*

Yi-Shun Li − *Department of Materials and Optoelectronic Science, Center for Functional Polymers and Supramolecular Materials, National Sun Yat-Sen University, Kaohsiung 804, Taiwan*

Complete contact information is available at:
https://pubs.acs.org/10.1021/acsaem.4c02968

Notes

The authors declare no competing financial interest.

REFERENCES

(1) Zhou, L.; Cao, H.; Zhu, S.; Hou, L.; Yuan, C. Hierarchical micro-/mesoporous N- and O-enriched carbon derived from disposable cashmere: a competitive cost-effective material for high-performance electrochemical capacitors. *Green Chem.* **2015**, *17*, 2373−2382.

(2) Yuan, G.; Su, Y.; Zhang, X.; Gao, B.; Hu, J.; Sun, Y.; Li, W.; Zhang, Z.; Shakouri, M.; Pang, H. Charged organic ligands inserting/supporting the nanolayer spacing of vanadium oxides for high-stability/efficiency zinc-ion batteries. *Natl. Sci. Rev.* **2024**, *11*, nwae336.

(3) Samy, M. M.; Mohamed, M. G.; Sharma, S. U.; Chaganti, S. V.; Lee, J. T.; Kuo, S. W. An Ultrastable Tetrabenzonaphthalene-Linked conjugated microporous polymer functioning as a high-performance electrode for supercapacitors. *J. Taiwan Inst. Chem. Eng.* **2024**, *158*, No. 104750.

(4) Guo, X.; Xu, H.; Tang, Y.; Yang, Z.; Dou, F.; Li, W.; Li, Q.; Pang, H. Confining Iodine into Metal-Organic Framework Derived Metal-Nitrogen-Carbon for Long-Life Aqueous Zinc-Iodine Batteries. *Adv. Mater.* **2024**, *36*, No. 2408317.

(5) Chang, S. Y.; Elewa, A. M.; Mohamed, M. G.; Mekhemer, I. M. A.; Samy, M. M.; Zhang, K.; Chou, H. H.; Kuo, S. W. Rational design and synthesis of bifunctional Dibenzo [g,p] chrysene-based conjugated microporous polymers for energy storage and visible light-driven photocatalytic hydrogen evolution. *Mater. Today Chem.* **2023**, *33*, No. 101680.

(6) Mousa, A. O.; Chuang, C. H.; Kuo, S. W.; Mohamed, M. G. Strategic design and synthesis of ferrocene linked porous organic frameworks toward tunable CO_2 capture and energy storage. *Int. J. Mol. Sci.* **2023**, *24*, 12371.

(7) Samy, M. M.; Mohamed, M. G.; Kuo, S. W. Pyrene-functionalized tetraphenylethylene polybenzoxazine for dispersing single-walled carbon nanotubes and energy storage. *Compos. Sci. Technol.* **2020**, *199*, No. 108360.

(8) Guo, X.; Xu, H.; Li, W.; Liu, Y.; Shi, Y.; Li, Q.; Pang, H. Embedding Atomically Dispersed Iron Sites in Nitrogen-Doped Carbon Frameworks-Wrapped Silicon Suboxide for Superior Lithium Storage. *Adv. Sci.* **2023**, *10*, No. 2206084.

(9) Zhang, J.; Wu, D.; Zhang, Q.; Zhang, A.; Sun, J.; Hou, L.; Yuan, C. Green self-activation engineering of metal−organic framework derived hollow nitrogen-doped carbon spheres towards super-capacitors. *J. Mater. Chem. A* **2022**, *10*, 2932−2944.

(10) Zhang, Q.; Yue, P.; Jia, M.; Jia, J.; Ren, Y.; Li, G.; Sun, J.; Hou, L.; Chen, M.; Yuan, C. Construction of honeycomb-like N-doped porous carbon framework with effective aperture distribution toward advanced supercapacitors and sodium-ion batteries. *Chem. Eng. J.* **2024**, *500*, No. 156779.

(11) Ram, M.; Aghahosseini, A.; Breyer, C. Job creation during the global energy transition towards 100% renewable power system by 2050. *Technol. Forecast. Soc. Change* **2020**, *151*, No. 119682.

(12) Mohamed, M. G.; Sharma, S. U.; Wang, P. T.; Ibrahim, M.; Lin, M. H.; Liu, C. L.; Ejaz, M.; Yen, H. J.; Kuo, S. W. Construction of Fully π-Conjugated, Diyne-Linked Conjugated Microporous Polymers Based on Tetraphenylethene and Dibenzo [g, p] chrysene Units for Energy Storage. *Polym. Chem.* **2024**, *15*, 2827−2839.

(13) Mousa, A. O.; Lin, Z. I.; Chaganti, S. V.; Chuang, C. H.; Chen, C. K.; Kuo, S. W.; Mohamed, M. G. Bifunctional imidazolium linked tetraphenylethene based conjugated microporous polymers for dynamic antibacterial properties and supercapacitor electrodes. *Polym. Chem.* **2024**, *15*, 397−411.

(14) Singh, P. N.; Mohamed, M. G.; Kuo, S. W. Systematic Design and Synthesis of Conjugated Microporous Polymers Containing Pyrene and Azobenzene Building Materials for High-Performance Energy Storage. *ACS Appl. Energy Mater.* **2023**, *6*, 11342−11351.

(15) Ejaz, M.; Mohamed, M. G.; Huang, W. C.; Kuo, S. W. Pyrene-based covalent organic polymers with nano carbonaceous composites for efficient supercapacitive energy storage. *J. Mater. Chem. A* **2023**, *11*, 22868−22883.

(16) Khan, H. R.; Ahmad, A. L. Supercapacitors: Overcoming current limitations and charting the course for next-generation energy storage. *J. Ind. Eng. Chem.* **2025**, *141*, 46−66.

(17) Olabi, A. G.; Abbas, Q.; Al Makky, A.; Abdelkareem, M. A. Supercapacitors as next generation energy storage devices: Properties and applications. *Energy* **2022**, *248*, No. 123617.

(18) Mousavi, S. M.; Hashemi, S. A.; Kalashgrani, M. Y.; Gholami, A.; Binazadeh, M.; Chiang, W. H.; Rahman, M. M. Recent advances in energy storage with graphene oxide for supercapacitor technology. *Sustainable Energy Fuels* **2023**, *7*, 5176−5197.

(19) Benoy, S. M.; Pandey, M.; Bhattacharjya, D.; Saikia, B. K. Recent trends in supercapacitor-battery hybrid energy storage devices based on carbon materials. *J. Energy Storage* **2022**, *52*, No. 104938.

(20) Castro-Gutiérrez, J.; Celzard, A.; Fierro, V. Energy storage in supercapacitors: Focus on tannin-derived carbon electrodes. *Front. Mater.* **2020**, *7*, 217.

(21) Mousa, A. O.; Mohamed, M. G.; Lin, Z. I.; Chuang, C. H.; Chen, C. K.; Kuo, S. W. Conjugated microporous polymers as a novel generation of drug carriers: A systemic study toward efficient carriers of tetracycline antibiotic. *Eur. Polym. J.* **2023**, *196*, No. 112254.

(22) Mohamed, M. G.; EL-Mahdy, A. F. M.; Kotp, M. G.; Kuo, S. W. Advances in porous organic polymers: Syntheses, structures, and diverse applications. *Mater. Adv.* **2022**, *3*, 707−733.

(23) Lee, J. S. M.; Cooper, A. I. Advances in Conjugated Microporous Polymers. *Chem. Rev.* **2020**, *120*, 2171−2214.

(24) Chaganti, S. V.; Sharma, S. U.; Ibrahim, M.; Basit, A.; Singh, P. N.; Kuo, S. W.; Mohamed, M. G. Redox-active a pyrene-4,5,9,10-tetraone and thienyltriazine-based conjugated microporous polymers for boosting faradaic supercapacitor energy storage. *J. Power Sources* **2025**, *627*, No. 235848.

(25) Luo, S.; Zeng, Z.; Zeng, G.; Liu, Z.; Xiao, R.; Xu, P.; Wang, H.; Huang, D.; Liu, Y.; Shao, B.; Liang, Q.; Wang, D.; He, Q.; Qin, L.; Fu, Y. Recent advances in conjugated microporous polymers for photocatalysis: designs, applications, and prospects. *J. Mater. Chem. A* **2020**, *8*, 6434−6470.

(26) Said, A. I.; Mohamed, M. G.; Madhu, M.; Singh, P. N.; Chaganti, S. V.; Elsayed, M. H.; Tseng, W. L.; Raymo, F. M.; Kuo, S. W. Bifunctional luminescent conjugated microporous polymers containing BODIPY and tetraphenylethene units for highly efficient energy storage and enhanced sensing of Cu^{2+} ions. *Polymer* **2024**, *300*, No. 126988.

(27) Mousa, A. O.; Mohamed, M. G.; Lin, Z. I.; Chuang, C. H.; Chen, C. K.; Kuo, S. W. Construction of cationic conjugated microporous polymers containing pyrene units through post-cationic modification for enhanced antibacterial performance. *J. Taiwan Inst. Chem. Eng.* **2024**, *157*, No. 105448.

(28) Mohamed, M. G.; Elsayed, M. H.; Li, C. J.; Hassan, A. E.; Mekhemer, I. M. A.; Musa, A. F.; Hussien, M. K.; Chen, L. C.; Chen, K. H.; Chou, H. H.; Kuo, S. W. Reticular design and alkyne bridge engineering in donor−π−acceptor type conjugated microporous polymers for boosting photocatalytic hydrogen evolution. *J. Mater. Chem. A* **2024**, *12*, 7693−7710.

(29) Mohamed, M. G.; Hu, H. Y.; Santhoshkumar, S.; Madhu, M.; Mansoure, T. H.; Hsiao, C. W.; Ye, Y.; Huang, C. W.; Tseng, W. L.; Kuo, S. W. Design and synthesis of bifunctional conjugated microporous polymers containing tetraphenylethene and bisulfone units for energy storage and fluorescent sensing of p-nitrophenol. *Colloids Surf. A: Physicochem. Eng. Asp.* **2024**, *680*, No. 132675.

(30) Mohamed, M. G.; Hu, H. Y.; Madhu, M.; Ejaz, M.; Sharma, S. U.; Tseng, W. L.; Samy, M. M.; Huang, C. W.; Lee, J. T.; Kuo, S. W. Construction of ultrastable conjugated microporous polymers containing thiophene and fluorene for metal ion sensing and energy storage. *Micromachines* **2022**, *13*, 1466.

(31) Mohamed, M. G.; Sharma, S. U.; Yang, C. H.; Samy, M. M.; Mohammed, A. A. K.; Chaganti, S. V.; Lee, J. T.; Wei-Kuo, S. Anthraquinone-enriched conjugated microporous polymers as organic cathode materials for high-performance lithium-ion batteries. *ACS Appl. Energy Mater.* **2021**, *4*, 14628−14639.

(32) Madhu, M.; Santhoshkumar, S.; Hsiao, C. W.; Tseng, W. L.; Kuo, S. W.; Mohamed, M. G. Selective and Sensitive Detection of Fe^{3+} Ions Using a Red-Emissive Fluorescent Probe Based on Triphenylamine and Perylene-Linked Conjugated Microporous Polymer. *Macromol. Rapid Commun.* **2024**, *45*, 2400263.

(33) Hsiao, C. W.; Elewa, A. M.; Mohamed, M. G.; Kotp, M. G.; Chou, M. M. C.; Kuo, S. W. Designing strategically functionalized

hybrid porous polymers with octavinylsilsesquioxane/dibenzo [g,p] chrysene/benzo [c]-1, 2, 5-thiadiazole units for rapid removal of Rhodamine B dye from water. *Colloids Surf. A: Physicochem. Eng. Asp.* **2024**, *699*, No. 134658.

(34) Sharma, S. U.; Elsayed, M. H.; Mekhemer, I. M. A; Meng, T. S.; Chou, H. H.; Kuo, S. W.; Mohamed, M. G. Rational design of pyrene and thienyltriazine-based conjugated microporous polymers for high-performance energy storage and visible-light photocatalytic hydrogen evolution from water. *Giant* **2024**, *17*, No. 100217.

(35) Mohamed, M. G.; Ibrahim, M.; Chen, N. P.; Basit, A.; Kao, A. Y. C.; Mousa, A. O.; Samy, M. M.; Kuo, S. W. Tetrabenzonaphthalene and Redox-Active Anthraquinone-Linked Conjugated Microporous Polymers as Organic Electrodes for Enhanced Energy Storage Efficiency. *ACS Appl. Energy Mater.* **2024**, *7*, 5582−5593.

(36) Lian, L.; Li, K.; Ren, L.; Han, D.; Lv, X.; Wang, H. G. Imine-linked triazine-based conjugated microporous polymers/carbon nanotube composites as organic anode materials for lithium-ion batteries. *Colloids Surf. A: Physicochem. Eng. Asp.* **2023**, *657*, No. 130496.

(37) Lee, J. S. M.; Wu, T. H.; Alston, B. M.; Briggs, M. E.; Hasell, T.; Hu, C. C.; Cooper, A. I. Porosity-engineered carbons for supercapacitive energy storage using conjugated microporous polymer precursors. *J. Mater. Chem. A* **2016**, *4*, 7665−7673.

(38) Osman, S.; Senthil, R. A.; Pan, J.; Li, W. Highly activated porous carbon with 3D microspherical structure and hierarchical pores as greatly enhanced cathode material for high-performance supercapacitors. *J. Power Sources* **2018**, *391*, 162−169.

(39) Khan, A.; Senthil, R. A.; Pan, J.; Osman, S.; Sun, Y.; Shu, X. A new biomass derived rod-like porous carbon from tea-waste as inexpensive and sustainable energy material for advanced supercapacitor application. *Electrochim. Acta* **2020**, *335*, No. 135588.

(40) Zhao, Y.; Bu, N.; Shao, H.; Zhang, Q.; Feng, B.; Xu, Y.; Zheng, G.; Yuan, Y.; Yan, Z.; Xia, L. A carbonized porous aromatic framework to achieve customized nitrogen atoms for enhanced supercapacitor performance. *New J. Chem.* **2019**, *43*, 18158−18164.

(41) Li, H.; Li, J.; Thomas, A.; Liao, Y. Ultra-high surface area nitrogen-doped carbon aerogels derived from a schiff-base porous organic polymer aerogel for CO_2 storage and supercapacitors. *Adv. Funct. Mater.* **2019**, *29*, 1904785.

(42) Zhao, Y.; Xie, F.; Zhang, C.; Kong, R.; Feng, S.; Jiang, J. X. Porous carbons derived from pyrene-based conjugated microporous polymer for supercapacitors. *Microporous Mesoporous Mater.* **2017**, *240*, 73−79.

(43) Jiao, Y.; Ye, Z.; Wu, F.; Xie, A.; Zhao, W.; Wu, L.; Zhu, X.; Dong, W. Conjugate microporous polymer-derived conductive porous carbon nanoparticles with narrow pore-size distribution for electromagnetic interference shielding. *ACS Appl. Nano Mater.* **2020**, *3*, 4553−4561.

(44) Mohamed, M. G.; Su, B. X.; Kuo, S. W. Robust Nitrogen-Doped Microporous Carbon via Crown Ether-Functionalized Benzoxazine-Linked Porous Organic Polymers for Enhanced CO_2 Adsorption and Supercapacitor Applications. *ACS Appl. Mater. Interfaces* **2024**, *16*, 40858−40872.

(45) Tian, W.; Zhang, D. X.; Sun, H.; Shao, G.; Wang, S. Porous carbons: structure-oriented design and versatile applications. *Adv. Funct. Mater.* **2020**, *30*, No. 1909265.

(46) Reza, M. S.; Afroze, S.; Kuterbekov, K.; Kabyshev, A.; Zh. Bekmyrza, K.; Haque, M. N.; Islam, S. N.; Hossain, M. A.; Hassan, M.; Roy, H.; Islam, M. S.; Pervez, M. N.; Azad, A. K. Advanced applications of carbonaceous materials in sustainable water treatment, energy storage, and CO_2 capture: a comprehensive review. *Sustainability* **2023**, *15*, 8815.

(47) Sun, Y.; Guo, S.; Li, W.; Pan, J.; Fernandez, C.; Senthil, R. A.; Sun, X. A green and template-free synthesis process of superior carbon material with ellipsoidal structure as enhanced material for supercapacitors. *J. Power Sources* **2018**, *405*, 80−88.

(48) Vinodh, R.; Gopi, C. V. M.; Kummara, V. G. R.; Atchudan, R.; Ahamad, T.; Sambasivam, S.; Yi, M.; Obaidat, I. M.; Kim, H. J. A review on porous carbon electrode material derived from hypercross-linked polymers for supercapacitor applications. *J. Energy Storage* **2020**, *32*, No. 101831.

(49) Shi, X.; Zhang, S.; Chen, X.; Tang, T.; Mijowska, E. Three dimensional graphene/carbonized metal-organic frameworks based high-performance supercapacitor. *Carbon* **2020**, *157*, 55−63.

(50) Hong, S.; Kim, Y.; Kim, Y.; Suh, K.; Yoon, M.; Kim, K. Hierarchical Porous Carbon Materials Prepared by Direct Carbonization of Metal−Organic Frameworks as an Electrode Material for Supercapacitors. *Bull. Korean Chem. Soc.* **2021**, *42*, 309−314.

(51) Xu, Y.; Wu, S.; Ren, S.; Ji, J.; Yue, Y.; Shen, J. Nitrogen-doped porous carbon materials generated via conjugated microporous polymer precursors for CO_2 capture and energy storage. *RSC Adv.* **2017**, *7*, 32496−32501.

(52) Mousa, A. O.; Mohamed, M. G.; Chuang, C. H.; Kuo, S. W. Carbonized aminal-linked porous organic polymers containing pyrene and triazine units for gas uptake and energy storage. *Polymers* **2023**, *15*, 1891.

(53) Mohamed, M. G.; Ahmed, M. M.; Du, W. T.; Kuo, S. W. Meso/microporous carbons from conjugated hyper-crosslinked polymers based on tetraphenylethene for high-performance CO_2 capture and supercapacitor. *Molecules* **2021**, *26*, 738.

(54) Mohamed, M. G.; Chang, S. Y.; Ejaz, M.; Samy, M. M.; Mousa, A. O.; Kuo, S. W. Design and synthesis of bisulfone-linked two-dimensional conjugated microporous polymers for CO_2 adsorption and energy storage. *Molecules* **2023**, *28*, 3234.

(55) Mohamed, M. G.; Chen, T. C.; Kuo, S. W. Solid-State Chemical Transformations to Enhance Gas Capture in Benzoxazine-Linked Conjugated Microporous Polymers. *Macromolecules* **2021**, *54*, 5866−5877.

(56) Mousa, A. O.; Sharma, S. U.; Chaganti, S. V.; Mansoure, T. H.; Singh, P. N.; Ejaz, M.; Chuang, C. H.; Lee, J. T.; Kuo, S. W.; Mohamed, M. G. Designing strategically functionalized conjugated microporous polymers with pyrene and perylenetetracarboxylic dianhydride moieties with single-walled carbon nanotubes to enhance supercapacitive energy storage efficiency. *J. Power Sources* **2024**, *608*, No. 234624.

(57) Kim, M.; Xin, R.; Earnshaw, J.; Tang, J.; Hill, J. P.; Ashok, A.; Nanjundan, A. K.; Kim, J.; Young, C.; Sugahara, Y.; Na, I.; Yamauchi, Y. MOF-derived nanoporous carbons with diverse tunable nano-architectures. *Nat. Prot.* **2022**, *17*, 2990−3027.

(58) Wang, Y.; Sun, S.; Wu, X.; Liang, H.; Zhang, Z. Status and opportunities of zinc ion hybrid capacitors: focus on carbon materials, current collectors, and separators. *Nanomicro Lett.* **2023**, *15*, 78.

(59) Gao, X.; Xiao, Z.; Jiang, L.; Wang, C.; Lin, X.; Sheng, L. Yolk-shell porous Fe_3O_4@ C anchored on graphene as anode for Li-ion half/full batteries with high rate capability and long cycle life. *J. Colloid Interface Sci.* **2023**, *641*, 820−830.

(60) Štěpnička, P. Ferrocene Chemistry. *Eur. J. Inorg. Chem.* **2022**, *2022*, No. e202200388.

(61) Zhou, B.; Liu, L.; Cai, P.; Zeng, G.; Li, X.; Wen, Z.; Chen, L. Ferrocene-based porous organic polymer derived high-performance electrocatalysts for oxygen reduction. *J. Mater. Chem. A* **2017**, *5*, 22163.

(62) Zhou, B.; Yan, F.; Li, X.; Zhou, J.; Zhang, W. An Interpenetrating Porous Organic Polymer as a Precursor for FeP/ Fe_2 P-Embedded Porous Carbon toward a pH-Universal ORR Catalyst. *ChemSusChem* **2019**, *12*, 915−923.

(63) Liu, X.; Liang, X.; Lou, H.; Wang, H.; Li, H.; Zhang, S.; Zhu, S.; Han, W.; Zhou, B. Ferrocene-based porous organic polymer derived N-doped porous carbon/Fe_3C nanocrystal hybrids towards high-efficiency ORR for Zn−air batteries. *Sustain Energy Fuels* **2021**, *5*, 1067.

(64) Wang, Y.; Tao, J.; Xiong, S.; Lu, P.; Tang, J.; He, J.; Javaid, M. U.; Pan, C.; Yu, G. Ferrocene-based porous organic polymers for high-affinity iodine capture. *Chem. Eng. J.* **2020**, *380*, No. 122420.

(65) Mohamed, M. G.; Elewa, A. M.; Li, M. S.; Kuo, S. W. Construction and multifunctional of hypercrosslinked porous organic polymers containing ferrocene unit for high-performance iodine

adsorption and supercapacitor. *J. Taiwan Inst. Chem. Eng.* **2023**, *150*, No. 105045.

(66) Zhuo, H.; Chen, W.; Yang, T.; Wei, C.; Li, W.; Feng, L.; Jin, T.; Fu, Z.; Chen, Y. Fe-doped N/S-rich carbon catalyst derived from porphyrine-ferrocene conjugated microporous polymer for bifunctional electrocatalysis and zinc-air batteries. *Appl. Catat. A, General* **2024**, *674*, No. 119617.

(67) Zhou, B.; Liu, L.; Cai, P.; Zeng, G.; Li, X.; Wen, Z.; Chen, L. Ferrocene-based Porous Organic Polymers Derived High-performance Electrocatalysts for Oxygen Reduction. *J. Mater. Chem. A* **2017**, *S*, 22163−22169.

(68) Mohamed, M. G.; Chen, C. C.; Ibrahim, M.; Mousa, A. O.; Elsayed, M. H.; Ye, Y.; Kuo, S. W. Tetraphenylanthraquinone and Dihydroxybenzene-Tethered Conjugated Microporous Polymer for Enhanced CO_2 Uptake and Supercapacitive Energy Storage. *JACS Au* **2024**, *4*, 3593−3605.

(69) Basit, A.; Mohamed, M. G.; Sharma, S. U.; Kuo, S. W. Thianthrene- and Thianthrene Tetraoxide-Functionalized Conjugated Microporous Polymers for Efficient Energy Storage. *ACS Appl. Polym. Mater.* **2024**, *6*, 12247−12260.

(70) Basit, A.; Mohamed, M. G.; Ejaz, M.; Su, B. X.; Manzoor, H.; Kuo, S. W. Boosting Supercapacitor Energy Storage Using Microporous Carbon Derived from an Octavinylsilsesquioxane and Fluorenone-Linked Porous Hybrid Polymer. *ACS Appl. Energy Mater.* **2024**, *7*, 7505−7516.